



# A bidirectional model for communication in the neurovascular unit

Alexandra Witthoft<sup>a</sup>, George Em Karniadakis<sup>b,\*</sup>

<sup>a</sup> School of Engineering, Brown University, Providence, RI 02912, USA

<sup>b</sup> Division of Applied Mathematics, Brown University, Providence, RI 02912, USA

## HIGHLIGHTS

- ▶ We model bidirectional signaling between cerebral astrocytes and microvessels.
- ▶ We construct a model of stretch-gated ion channels in perivascular astrocyte endfeet.
- ▶ Vessel dilations provoke astrocyte calcium increases and membrane depolarization.
- ▶ Astrocyte-induced vasodilation inhibits vasomotion via hyperpolarization.
- ▶ We validate our model predictions with in vitro and in vivo data.

## ARTICLE INFO

### Article history:

Received 20 January 2012

Received in revised form

9 July 2012

Accepted 13 July 2012

Available online 22 July 2012

### Keywords:

Neurovascular coupling

TRP channels

Astrocytes

## ABSTRACT

The neurovascular unit is a coordinated and interactional system of neurons, astrocytes, and microvessels in the brain. A central autoregulation mechanism observed in this unit is functional hyperemia, in which the microvasculature dilates in response to local neural activity in order to meet the increased demand for blood flow and oxygen. We have developed the first interactional model of bidirectional signaling in the neurovascular unit. The vascular model includes a description of vasomotion, the vascular oscillatory response to transmural pressure, observed in vivo. The communication mechanisms in the model include neural synaptic glutamate and potassium signaling to the astrocytes, potassium signaling from the astrocyte to the microvasculature, and astrocytic mechanosensation of vascular changes. The model response of the astrocyte to arteriolar dilation is validated with recent in vivo and in vitro experimental results. The model reproduces for the first time the in vitro observed phenomenon in which arteriole radius and  $\text{Ca}^{2+}$  oscillations, “vasomotion,” are damped due to neural induced astrocytic signaling.

© 2012 Elsevier Ltd. All rights reserved.

## 1. Introduction

Recently, cerebral vasculature has been considered not as an isolated system but as being integrated with the brain in a coordinated, interactional, autoregulating neurovascular unit. An important mechanism in this interaction is functional hyperemia, in which the microvasculature dilates in response to local neural activity in order to meet the increased demand for blood flow. The dilation occurs after neural activity triggers a series of chemical and electrical reactions in adjacent astrocytes, glial cells with long extending processes whose endfeet wrap around arterioles and neural synapses (Haydon and Carmignoto, 2006; McCaslin et al., 2011; Halassa et al., 2007). Significant work has been done investigating the vascular response to neural and astrocytic inputs (Bennett et al., 2008; Farr and David, 2011; Filosa et al.,

2004) but very little has been done to explore the effect that vascular activities may have on neurons and astrocytes. The hemo-neural hypothesis, proposed by Moore and Cao (2008), implies that the cerebral vasculature has pivotal effects on neural function through a variety of direct and indirect mechanisms. We suggest that one of these indirect mechanisms is activated by astrocytic mechanosensation of vascular motions. Cerebral astrocytes have been shown to express the transient receptor potential vanilloid-related channel 4 (TRPV4), a mechanosensitive cation channel, and these have been observed to be particularly abundant in astrocytic processes facing blood vessels (Benfenati et al., 2007). There has also been experimental documentation in vitro and in vivo of astrocytic depolarization and intracellular calcium increase in response to vessel dilations (Cao, 2011), both of which could be explained by TRPV4 channel activity.

We present an interactional model of bidirectional signaling in the neurovascular unit. This is the first computational model of astrocyte response to vascular function, making it the first model of a neurovascular unit to include a two-way communication path

\* Corresponding author. Tel.: +1 401 8631217.

E-mail address: [gk@dam.brown.edu](mailto:gk@dam.brown.edu) (G. Em Karniadakis).

between the brain and vasculature. A previous model for the astrocyte signaling cascade, in which the astrocyte signals to the arteriole by releasing epoxyeicosatrienoic acid (EET), has been reported by Bennett et al. (2008). Since then, Farr and David (2011) developed this model further to include an EET-dependent potassium ( $K^+$ ) release, which activated inward-rectifier potassium (KIR) channels in the arteriole smooth muscle cell (SMC), leading to SMC relaxation and vasodilation. We adapt these models along with a model for small arteries by Gonzalez-Fernandez and Ermentrout (1994) that takes into account the viscoelastic nature of the arteriole wall along with its electrical and biochemical properties. Here, we combine and significantly extend the models of Gonzalez-Fernandez and Ermentrout (1994), Bennett et al. (2008), and Farr and David (2011) by adding a signaling mechanism in the reverse direction – from vessels to astrocytes – resulting in the first bidirectional neurovascular model. This is also the first model to predict the interactions of astrocytes with vessels experiencing vasomotion.

## 2. Theory

### 2.1. Overview of the model

The neurovascular unit contains the brain, the cerebral vessels and microvasculature, and glial cells. The astrocytes are star-shaped glial cells whose long processes terminate in endfeet that wrap around arterioles and neural synapses. While astrocytes have been observed to signal to one another (Halassa et al., 2007; McCaslin et al., 2011), astrocytes processes do not overlap with those of another astrocyte, so the brain is spatially mapped into a 3D grid of distinct “astrocyte domains,” where each astrocyte may have sole influence over all the synapses within its domain (Nedergaard et al., 2003; Halassa et al., 2007). For this model, we consider a single astrocyte domain, and in order to study in isolation the direct two-way signaling path between astrocytes and vessels, we leave out astrocyte-to-astrocyte signaling. For simplicity, we consider only the net neural synaptic activity across the entire astrocyte domain, and assume this activity to be uniform throughout the domain.

A conceptual diagram of the proposed model is shown in Fig. 1. A corresponding overview plot of the interaction mechanisms included in our model is given in Fig. 2. The perisynaptic endfoot and synaptic space in the diagram represent the sum of the activities of all the synapses and perisynaptic endfeet associated with the astrocyte. During high synaptic activity in the region, the neurons release  $K^+$  ions and glutamate at the

synapses ( $\Omega_S$ ).  $K^+$  flows into the adjacent astrocytic endfoot depolarizing the astrocyte membrane. It should be noted that Farr and David (2011) refer to this current as the sodium-potassium (Na-K) pump current, but this is not entirely accurate. The Na-K pump is a mechanism present in the astrocyte synapse-adjacent processes that exchanges sodium ( $Na^+$ ) ions for  $K^+$  ions: three  $Na^+$  ions are released for every two  $K^+$  ions that enter the astrocyte. Thus, the electrical flux from the Na-K pump would actually hyperpolarize the membrane. The depolarization happens because there is an additional  $K^+$  influx through KIR channels present in the astrocyte processes (Barres et al., 1990; Higashi et al., 2001; Higashimori and Sontheimer, 2007). When Farr and David (2011) refer to the Na-K flux,  $J_{NaK}$ , they are probably referring to the combined potassium flux from the Na-K pump and the KIR channels. Here, for clarity, we will call this combined flux  $J_{\Sigma K}$ .

The synaptic glutamate binds to metabotropic receptors (mGluR) on the astrocyte endfoot, initiating a G-protein cascade in which  $IP_3$  is produced inside the astrocyte wall ( $\Omega_{Astr}$ ). Inside

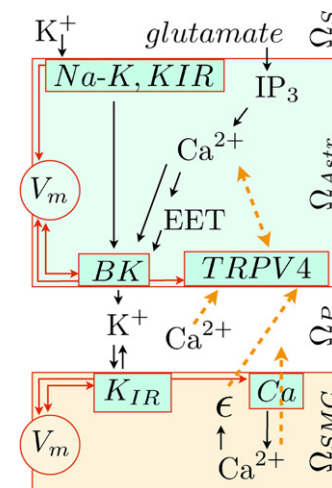


**Fig. 2.** Model flow chart. ( $\Omega_S$ )  $K^+$  and glutamate in the synaptic space. ( $\Omega_{Astr}$ )  $K^+$  influx depolarizes the membrane; glutamate receptor binding initiates the reaction cascade  $IP_3$ , internal  $Ca^{2+}$  release, EET.  $Ca^{2+}$  and EET open BK channels. TRPV4  $Ca^{2+}$  influx is activated by vessel dilation (strain,  $\epsilon$ ), and inhibited by intra- and extracellular  $Ca^{2+}$ . ( $\Omega_P$ )  $K^+$  accumulates from astrocyte BK and SMC KIR flux.  $Ca^{2+}$  concentration is affected by SMC  $Ca^{2+}$  flux. ( $\Omega_{SMC}$ ) Extracellular  $K^+$  activates KIR channels, hyperpolarizing the membrane, closing  $Ca^{2+}$  channels. Reduced  $Ca^{2+}$  influx causes myogenic dilation,  $\epsilon$ . Dashed arrows indicate new mechanisms we have formulated in this model.

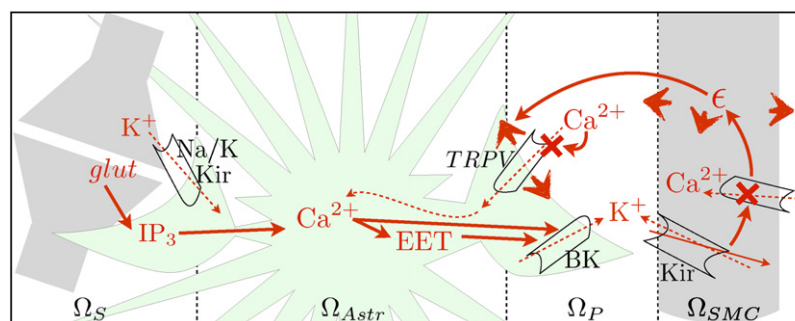


**Fig. 1.** Model overview.  $\Omega_S$ , Synaptic space—active synapses release glutamate and  $K^+$ .  $K^+$  enters the astrocyte through Na-K pump and KIR channels. Glutamate binds to metabotropic receptors on the astrocyte endfoot.  $\Omega_{Astr}$ , astrocyte intracellular space—bound glutamate receptors effect  $IP_3$  production inside the astrocyte wall, leading to release of  $Ca^{2+}$  from internal stores, causing EET production.  $Ca^{2+}$  and EET open BK channels at the perivascular endfoot, releasing  $K^+$  into the perivascular space ( $\Omega_P$ ).  $\Omega_{SMC}$ , arteriole smooth muscle cell intracellular space—KIR channels in the arteriolar SMC are activated by the increase in extracellular  $K^+$ . The resulting drop in membrane potential closes  $Ca^{2+}$  channels, reducing  $Ca^{2+}$  influx, leading to SMC relaxation. The arteriole dilation (strain,  $\epsilon$ ) stretches the membrane of the enclosing astrocyte perivascular endfoot, which activates  $Ca^{2+}$  influx through TRPV4 channels. Note that the diagram here is not to scale. The perivascular endfoot is actually in contact with the arteriole and wraps around its circumference, but we show them separated here in order to detail the ion flow at the endfoot-vessel interface.

the astrocyte, IP<sub>3</sub> binds to receptors (IP<sub>3</sub>R) on the endoplasmic reticulum (ER), releasing internal stores of calcium ions (Ca<sup>2+</sup>). The rise in intracellular Ca<sup>2+</sup> enables production of EET, and EET and Ca<sup>2+</sup> activate BK channels in the vessel-adjacent astrocyte endfoot, releasing K<sup>+</sup> into the perivascular space (Ω<sub>p</sub>). The K<sup>+</sup> buildup in the perivascular space activates KIR channels in the arteriolar smooth muscle cell (SMC) (Ω<sub>SMC</sub>). Unlike the astrocyte KIR channels on the synapse-adjacent processes, SMC KIR channels have a reversal potential much lower than the SMC membrane potential, so the K<sup>+</sup> flows outward. The resulting membrane voltage drop closes inward Ca<sup>2+</sup> channels, and the intracellular Ca<sup>2+</sup> concentration in the SMC drops. Because Ca<sup>2+</sup> is required for myosin-actin crossbridge attachment, the crossbridges then detach, allowing the SMC to relax and the arteriole to expand. As the vessel expands, it stretches the perivascular astrocyte endfoot encircling it (Ω<sub>Astr</sub>), opening stretch-gated Ca<sup>2+</sup>-permeable TRPV4 channels in the endfoot. As a result, the astrocyte experiences a membrane depolarization and a rise in intracellular Ca<sup>2+</sup> due to an influx of Ca<sup>2+</sup> through the TRPV4 channels. The Ca<sup>2+</sup> influx has a cumulative effect on the BK channels, which prolongs the K<sup>+</sup> signal (Ω<sub>p</sub>) to the arteriole (Ω<sub>SMC</sub>).

Given that the arteriole movements stretch the membrane of the enclosing astrocyte endfoot, it is worth mentioning the possibility of mechanical feedback to the arteriole, which is not addressed specifically in this model. Because the parameters in the arteriole model were calibrated to in vivo data, we can consider the mechanical model for the vascular SMC as a lumped model that treats the viscoelastic arteriole wall and the enclosing astrocyte endfeet as a single viscoelastic structure.

## 2.2. Synaptic space, Ω<sub>s</sub>

When neurons are activated, they release K<sup>+</sup> and glutamate into the synaptic space (Fig. 2). The governing equation for the potassium in the synaptic space is (Farr and David, 2011)

$$\frac{d[K^+]_s}{dt} = J_{K_s} - J_{\Sigma K}, \quad (1)$$

where  $J_{K_s}$  is a smooth pulse approximation of potassium release from active neurons. The combined Na–K pump and KIR flux out of the synaptic space and into the astrocyte,  $J_{\Sigma K}$ , is

$$J_{\Sigma K} = J_{\Sigma K, \max} k_{Na} \frac{[K^+]_s}{[K^+]_s + K K o_a}. \quad (2)$$

This equation actually models the Na–K pump flux (Farr and David, 2011), but their chosen value for  $J_{\Sigma K, \max}$ , the maximum flux, gives a large enough value for  $J_{\Sigma K}$  to represent the combined activity of the Na–K pump and KIR channels. Thus, we are using the Na–K pump model as a lumped model for both fluxes. The potassium concentration in the synaptic space is  $[K^+]_s$ , and  $K K o_a$  is the threshold value for  $[K^+]_s$ . For simplicity, the extracellular sodium concentration,  $[Na^+]_s$ , is assumed to be constant, so the parameter  $k_{Na}$  comes from  $k_{Na} = [Na^+]_s^{1.5} / ([Na^+]_s^{1.5} + K N a_s^{1.5})$ , where  $K N a_s$  is the threshold value for  $[Na^+]_s$  (Farr and David, 2011).

The synaptic glutamate release is assumed to be a smooth pulse, and the ratio of active to total G-protein due to mGluR binding on the astrocyte endfoot is given by

$$G^* = \frac{\rho + \delta}{K_G + \rho + \delta}, \quad (3)$$

where  $\rho = [Glu] / (K_{Glu} + [Glu])$  is the ratio of bound to unbound receptors, and  $\delta$  is the ratio of the activities of bound and unbound receptors, which allows for background activity in the absence of a stimulus (Bennett et al., 2008).

## 2.3. Astrocytic intracellular space, Ω<sub>Astr</sub>

The influx of synaptic potassium into the astrocyte causes a membrane depolarization. Meanwhile, astrocytic IP<sub>3</sub> production occurs inside the cell wall in response to synaptic glutamate binding to metabotropic receptors. IP<sub>3</sub> causes release of intracellular Ca<sup>2+</sup>, which both inhibits TRPV4 channels and triggers EET production. Both Ca<sup>2+</sup> and EET activate the astrocytic BK channels, which release K<sup>+</sup> into the perivascular space. In addition, vessel dilation (strain,  $\epsilon$ ) activates the TRPV4 channels, allowing an influx of Ca<sup>2+</sup> into the astrocyte.

The IP<sub>3</sub> production in the astrocyte is based on the model by Bennett et al. (2008) as modified by Farr and David (2011):

$$\frac{d[IP_3]}{dt} = r_h^* G^* - k_{deg}[IP_3], \quad (4)$$

where  $r_h^*$  is the IP<sub>3</sub> production rate and  $k_{deg}$  is the degradation rate.

The astrocytic intracellular Ca<sup>2+</sup> comes from both external influx, through TRPV4 channels at the perivascular interface, and release of internal stores in the endoplasmic reticulum (ER):

$$\frac{d[Ca^{2+}]}{dt} = \beta (J_{IP_3} - J_{pump} + J_{leak} + J_{TRPV}), \quad (5)$$

where  $[Ca^{2+}]$  is the cytosolic calcium concentration,  $\beta$  is the factor describing Ca<sup>2+</sup> buffering, and  $J_{TRPV}$  is the Ca<sup>2+</sup> influx from extracellular space through TRPV4 channels (see Eq. (10) below). The calcium stores in the ER have three mechanisms for calcium transport: (1) IP<sub>3</sub>R receptors on the ER bind to intracellular IP<sub>3</sub>, initiating Ca<sup>2+</sup> outflux from the ER,  $J_{IP_3}$ , into the intracellular space; (2) a pump uptakes Ca<sup>2+</sup> from the cytosol into the ER,  $J_{pump}$ , and (3) a leak flux  $J_{leak}$  from the ER into the intracellular space (Bennett et al., 2008). The IP<sub>3</sub>-dependent current is

$$J_{IP_3} = J_{max} \left[ \left( \frac{[IP_3]}{[IP_3] + K_I} \right) \left( \frac{[Ca^{2+}]}{[Ca^{2+}] + K_{act}} \right) h \right]^3 \left( 1 - \frac{[Ca^{2+}]}{[Ca^{2+}]_{ER}} \right), \quad (6)$$

where  $J_{max}$  is the maximum rate,  $K_I$  is the dissociation constant for IP<sub>3</sub>R binding,  $K_{act}$  is the dissociation constant for Ca<sup>2+</sup> binding to an activation site on the IP<sub>3</sub>R, and  $[Ca^{2+}]_{ER}$  is the Ca<sup>2+</sup> concentration in the ER. The gating variable  $h$  is governed by

$$\frac{dh}{dt} = k_{on}[K_{inh} - ([Ca^{2+}] + K_{inh})h], \quad (7)$$

where  $k_{on}$  and  $K_{inh}$  are the Ca<sup>2+</sup> binding rate and dissociation constant, respectively, at the inhibitory site on the IP<sub>3</sub>R. The pump flux is

$$J_{pump} = V_{max} \frac{[Ca^{2+}]^2}{[Ca^{2+}]^2 + K_p^2}, \quad (8)$$

where  $V_{max}$  is the maximum pump rate and  $K_p$  is the pump constant. The leak channel flux is

$$J_{leak} = P_L \left( 1 - \frac{[Ca^{2+}]}{[Ca^{2+}]_{ER}} \right), \quad (9)$$

where  $P_L$  is determined by the steady-state flux balance. The calcium influx from extracellular space,  $J_{TRPV}$ , is determined by the arteriolar tone at the location where the astrocyte endfoot encloses the microvessel. The electrical current through the channel is

$$I_{TRPV} = g_{TRPV} S (V_k - v_{TRPV}), \quad (10)$$

where  $g_{TRPV}$  is the maximum channel conductance,  $v_{TRPV}$  is the channel reversal potential, and  $V_k$  is the membrane potential (see Eq. (20) below). The calcium ion flux through the channel is given by  $J_{TRPV} = -I_{TRPV} / (C_{astr} \gamma)$ , where  $C_{astr}$  is the astrocyte cell capacitance, and  $\gamma$  is a scaling factor for relating the net movement of ion fluxes to the membrane potential (Koenigsberger et al., 2006).

There is a factor of  $-1$  because  $J_{TRPV}$  is a flux of positive ions, whereas electrical current,  $I_{TRPV}$ , always describes the motion of negative charges (an outflux of electrons being equivalent to an influx of positive ions).

The TRPV4 channel current is activated by mechanical stretches, and, after activation stops, experiences a slow decay in the absence of extracellular  $\text{Ca}^{2+}$ , and a fast decay in the presence of high extracellular  $\text{Ca}^{2+}$  (Nilius et al., 2004; Watanabe et al., 2003). Thus, we model the open probability as an ODE that decays to its variable steady state,  $s_\infty$  (Eq. (12), below), according to

$$\frac{ds}{dt} = \frac{1}{\tau_{Ca}([Ca^{2+}]_p)}(s_\infty - s), \quad (11)$$

where the  $\text{Ca}^{2+}$ -dependent time constant  $\tau_{Ca}([Ca^{2+}]_p) = \tau_{TRPV}/[Ca^{2+}]_p$ , where  $[Ca^{2+}]_p$  is the perivascular  $\text{Ca}^{2+}$  concentration (Eq. (23), below) expressed in  $\mu\text{M}$ , and  $s_\infty$  is the strain- and  $\text{Ca}^{2+}$ -dependent steady-state channel open probability. We model this with the Boltzmann equation (Hamill and Martinac, 2001; Koenigsberger et al., 2006):

$$s_\infty = \left( \frac{1}{1 + e^{-(\epsilon - \epsilon_{1/2})/\kappa}} \right) \left[ \frac{1}{1 + H_{Ca}} \left( H_{Ca} + \tanh \left( \frac{V_k - v_{1,TRPV}}{v_{2,TRPV}} \right) \right) \right]. \quad (12)$$

The first term  $1/(1 + e^{-(\epsilon - \epsilon_{1/2})/\kappa})$  describes the material strain gating, adapted from Koenigsberger et al. (2006). The strain on the perivascular endfoot,  $\epsilon$ , is taken to be the same as the local radial strain on the arteriole  $\epsilon = (r - r_0)/r_0$  (see Eq. (A.12) in Appendix A), while  $\epsilon_{1/2}$  is the strain required for half-activation. The second term describes the voltage gating and  $\text{Ca}^{2+}$  inhibitory behavior, based on the experimental results from Watanabe et al. (2003) and Nilius et al. (2003). The inhibitory term,  $H_{Ca}$ , is

$$H_{Ca} = \left( \frac{[Ca^{2+}]_i}{\gamma_{Ca_i}} + \frac{[Ca^{2+}]_p}{\gamma_{Ca_e}} \right), \quad (13)$$

where  $[Ca^{2+}]_i$  is the astrocytic intracellular  $\text{Ca}^{2+}$  concentration (Eq. (5)),  $[Ca^{2+}]_p$  is the perivascular  $\text{Ca}^{2+}$  concentration (Eq. (23), below), and  $\gamma_{Ca_i}$  and  $\gamma_{Ca_e}$  are constants associated with intra- and extracellular  $\text{Ca}^{2+}$ , respectively.

The rise in intracellular  $\text{Ca}^{2+}$  in the astrocyte leads to EET production inside the cell. The EET production is governed by

$$\frac{d[\text{EET}]}{dt} = V_{EET}([Ca^{2+}] - [Ca^{2+}]_{min}) - k_{EET}[\text{EET}], \quad (14)$$

where  $V_{EET}$  is the EET production rate;  $[Ca^{2+}]_{min}$  is the minimum  $[Ca^{2+}]$  required for EET production, and  $k_{EET}$  is the EET decay rate. Following Farr and David (2011), we assume that EET acts only on the astrocyte BK channels in the perivascular endfoot, rather than acting directly on the arteriole SMC as in Bennett et al. (2008).

Astrocytic BK channels, which occur on the perivascular end-foot, are affected by both EET and  $\text{Ca}^{2+}$ , as described by Farr and David (2011). The BK channel current is

$$I_{BK} = g_{BK} n_{BK} (V_k - v_{BK}), \quad (15)$$

where  $g_{BK}$  is the channel conductance,  $v_{BK}$  is the reversal potential, and  $n_{BK}$  is governed by

$$\frac{dn_{BK}}{dt} = \phi_{BK} (n_\infty [BK] - n_{BK}), \quad (16)$$

with

$$\phi_{BK} = \psi_{BK} \cosh \left( \frac{V_k - v_{3,BK}}{2v_{4,BK}} \right), \quad (17)$$

$$n_{\infty, BK} = 0.5 \left( 1 + \tanh \left( \frac{V_k + EET_{shift}[\text{EET}] - v_{3,BK}}{v_{4,BK}} \right) \right). \quad (18)$$

Also  $v_{3,BK}$  is the potential associated with 1/2 open probability, which depends on  $[Ca^{2+}]$ :

$$v_{3,BK} = -\frac{v_{5,BK}}{2} \tanh \left( \frac{[Ca^{2+}] - Ca_{3,BK}}{Ca_{4,BK}} \right) + v_{6,BK}, \quad (19)$$

where  $v_{4,BK}$ ,  $v_{5,BK}$ ,  $v_{6,BK}$ ,  $Ca_{3,BK}$ ,  $Ca_{4,BK}$ , and  $\psi_{BK}$  are constants, and  $EET_{shift}$  determines the EET-dependent shift of the channel reversal potential.

The astrocyte membrane potential is described by

$$\frac{dV_k}{dt} = \frac{1}{C_{astr}} (-I_{BK} - I_{leak} - I_{TRPV} - I_{\Sigma K}), \quad (20)$$

where  $I_{\Sigma K}$  is the electrical current carried by the  $K^+$  influx at the perisynaptic process:  $I_{\Sigma K} = J_{\Sigma K} C_{astr} \gamma$  (see Eq. (2)). The leak current,  $I_{leak}$ , is

$$I_{leak} = g_{leak} (V_k - v_{leak}), \quad (21)$$

where  $g_{leak}$  and  $v_{leak}$  are the leak conductance and reversal potential, respectively.

#### 2.4. Perivascular space, $\Omega_p$

The perivascular space experiences a buildup of  $K^+$  due to outflow from the astrocyte and smooth muscle cell intracellular spaces (Fig. 2). The perivascular  $K^+$  activates SMC KIR channels. Additionally,  $\text{Ca}^{2+}$  currents from the SMC affect the perivascular  $\text{Ca}^{2+}$  concentration, which has an inhibitory effect on the astrocyte TRPV4 channels.

The potassium accumulates in the perivascular space due to outflow from astrocytic BK channels and arteriolar smooth muscle cell KIR channels. The equation governing perivascular  $K^+$  comes from (Farr and David, 2011):

$$\frac{d[K^+]_p}{dt} = \frac{J_{BK}}{VR_{pa}} + \frac{J_{KIR}}{VR_{ps}} - R_{decay}([K^+]_p - [K^+]_{p,min}), \quad (22)$$

where  $VR_{pa}$  and  $VR_{ps}$  are the volume ratios of perivascular space to astrocyte and SMC, respectively, and  $[K^+]_{p,min}$  is the resting state equilibrium  $K^+$  concentration in the perivascular space.  $R_{decay}$  is the rate at which perivascular  $K^+$  concentration decays to its baseline state due to a combination of mechanisms including uptake in background cellular activity and diffusion through the extracellular space. The potassium flow from the astrocyte and SMC are  $J_{BK}$  and  $J_{KIR}$ , respectively, given as  $J_{BK} = I_{BK}/(C_{astr} \gamma)$ , and  $J_{KIR} = I_{KIR}/(C_{SMC} \gamma)$  (Eqs. (15) and (24)), where  $C_{SMC}$  is the SMC capacitance.

The perivascular  $\text{Ca}^{2+}$  concentration obeys

$$\frac{d[Ca^{2+}]_p}{dt} = -J_{TRPV} - J_{Ca} - Ca_{decay}([Ca^{2+}]_p - [Ca^{2+}]_{p,0}), \quad (23)$$

where  $J_{Ca}$  is the calcium current from the arteriole SMC (see Eq. (36) below), and  $Ca_{decay}$  is the decay rate of perivascular  $\text{Ca}^{2+}$  concentration (similar to  $R_{decay}$ ).

#### 2.5. Arteriole smooth muscle cell intracellular space, $\Omega_{SMC}$

The arteriole tone depends on the level of intracellular  $\text{Ca}^{2+}$  in the SMC (Fig. 2). When the SMC KIR channels are activated due to perivascular  $K^+$ , the SMC membrane potential experiences a hyperpolarization, which closes  $\text{Ca}^{2+}$  channels. The reduced  $\text{Ca}^{2+}$  influx results in a higher concentration of  $\text{Ca}^{2+}$  in the perivascular space. Also, the decreased  $\text{Ca}^{2+}$  level in the SMC intracellular space results in a dilation ( $\epsilon$ ), which then activates the astrocytic TRPV4 channels.

This vascular SMC model from Gonzalez-Fernandez and Ermentrout (1994) describes vasomotion as a result of pressure-sensitive  $\text{Ca}^{2+}$  ion channel activity in the SMC (see Eqs. (37) and (38), below). Other models assume that vasomotion is also

affected by endothelial cell activity (Koenigsberger et al., 2006; Farr and David, 2011). Both the SMC and endothelial cells are likely to have a contribution to vasomotion. However, there have been observations of vasomotion in arterioles in which the endothelium was removed (Haddock et al., 2002), indicating that the endothelium is not required for vasomotion, even if it can have an effect. Thus, for simplicity, we leave out the role of endothelial cells, but they can be added to the model at a later time.

### 2.5.1. Ion currents

The potassium buildup in the perivascular space activates the SMC KIR channels according to (Farr and David, 2011)

$$I_{KIR} = g_{KIR}k(V_m - v_{KIR}), \quad (24)$$

where the channel conductance,  $g_{KIR}$ , reversal potential,  $v_{KIR}$ , and open probability,  $k$ , all depend on the perivascular  $K^+$  concentration:

$$g_{KIR} = g_{KIR,0} \sqrt{[K^+]_p}, \quad (25)$$

where  $[K^+]_p$  is in units of mM, and  $g_{KIR,0}$  is the conductance when the perivascular  $K^+$  concentration is 1 mM;

$$v_{KIR} = v_{KIR,1} \log[K^+]_p - v_{KIR,2}, \quad (26)$$

where  $[K^+]_p$  is again in units of mM, and  $v_{KIR,1}$  and  $v_{KIR,2}$  are constants, and

$$\frac{dk}{dt} = \frac{1}{\tau_k} (k_\infty - k), \quad (27)$$

where  $\tau_k = 1/(\alpha_k + \beta_k)$ , and  $k_\infty = \alpha_k/(\alpha_k + \beta_k)$ , in which

$$\alpha_k = \frac{\alpha_{KIR}}{1 + \exp\left(\frac{V_m - v_{KIR} + a_{v1}}{a_{v2}}\right)}, \quad (28)$$

$$\beta_k = \beta_{KIR} \exp(b_{v2}(V_m - v_{KIR} + b_{v1})), \quad (29)$$

where  $\alpha_{KIR}$ ,  $\beta_{KIR}$ ,  $a_{v1}$ ,  $a_{v2}$ ,  $b_{v1}$ , and  $b_{v2}$  are constants (Farr and David, 2011). The SMC membrane potential is  $V_m$  (see Eq. (30), below).

The equations for the SMC dynamics are taken from Gonzalez-Fernandez and Ermentrout (1994) with the addition of the KIR current in Eq. (24). The SMC membrane potential obeys

$$\frac{dV_m}{dt} = \frac{1}{C_{SMC}} (-I_L - I_K - I_{Ca} - I_{KIR}), \quad (30)$$

where  $C_{SMC}$  is the cell capacitance, and  $I_L$ ,  $I_K$ , and  $I_{Ca}$  are the leak,  $K^+$  channel potassium, and calcium currents, respectively. The leak current is simply  $I_L = g_L(V_m - v_L)$ , where  $g_L$  is the leak conductance, and  $v_L$  is the leak reversal potential. The  $K^+$  channel current is

$$I_K = -g_K n (V_m - v_K), \quad (31)$$

where  $g_K$  and  $v_K$  are the channel conductance and reversal potential, respectively. The fraction of  $K^+$  channel open states,  $n$ , is described by

$$\frac{dn}{dt} = \lambda_n (n_\infty - n), \quad (32)$$

with

$$n_\infty = 0.5 \left( 1 + \tanh \frac{V_m - v_3}{v_4} \right), \quad (33)$$

and

$$\lambda_n = \phi_n \cosh \frac{V_m - v_3}{2v_4}, \quad (34)$$

where  $v_4$  is the spread of the open state distribution with respect to voltage, and  $v_3$  is the voltage associated with the opening of half the population, and is dependent on the  $Ca^{2+}$  concentration

in the SMC:

$$v_3 = -\frac{v_5}{2} \tanh \frac{[Ca^{2+}]_{SMC} - Ca_3}{Ca_4} + v_6. \quad (35)$$

The parameters  $Ca_3$  and  $Ca_4$  affect the shift and spread of the distribution, respectively, of  $v_3$  with respect to  $Ca^{2+}$ , and  $v_5$ ,  $v_6$  are constants. The  $Ca^{2+}$  channel current is

$$I_{Ca} = g_{Ca} m_\infty (V_m - v_{Ca}), \quad (36)$$

where  $g_{Ca}$  and  $v_{Ca}$  are the channel conductance and reversal potential, respectively. Since *fast kinetics* are assumed for the  $Ca^{2+}$  channel, the distribution of open channel states is equal to the equilibrium distribution

$$m_\infty = 0.5 \left( 1 + \tanh \frac{V_m - v_1}{v_2} \right), \quad (37)$$

with  $v_1$  and  $v_2$  having the same effect as  $Ca_3$  and  $Ca_4$  in Eq. (35) and  $v_3$  and  $v_4$  in Eq. (33). Note that in this case,  $v_1$  is a variable that depends on the transmural pressure. We represent the relationship using this linear approximation of the data from Gonzalez-Fernandez and Ermentrout (1994):

$$v_1 = -17.4 - 12\Delta P / 200, \quad (38)$$

where  $\Delta P$  is in units of mmHg, and  $v_1$  is in mV. For our model, we chose a value of 60 mmHg for  $\Delta P$ , which we found to be consistent with experimental observations (e.g. Hudetz et al., 1987, Fig. 5) for arterioles around 50  $\mu$ m in diameter, the size used in our simulations.

The SMC myogenic contractile behavior, which constricts the vessel, depends on the  $Ca^{2+}$  concentration in the SMC. The vessel circumference,  $x$ , is described by

$$\frac{dx}{dt} = \frac{1}{\tau} (f_{\Delta P} - f_x - f_u), \quad (39)$$

where  $\tau$  is the time constant, and  $f_{\Delta P}$ ,  $f_x$ , and  $f_u$  are the forces due to transmural pressure, viscoelasticity of the material, and myogenic response, respectively. The myogenic force,  $f_u$ , depends on the SMC  $Ca^{2+}$  concentration, which changes based on the  $Ca^{2+}$  ion channel current. These forces are discussed in detail in Appendix A.

## 3. Results

### 3.1. Simulation procedures

We simulated neural-induced vasodilation by representing the total synaptic activity in the astrocyte domain as a uniform, continuous smooth pulse of glutamate ( $[Glu]$ ) and of synaptic potassium ( $[K^+]_s$ ). For validation, we also simulated two experimental procedures following Cao (2011). In the first, we simulate astrocyte membrane depolarization in response to purely mechanical vessel dilations by imposing a time-dependent radial strain which we extracted from Cao (2011) and then interpolated (see Fig. 3).

In the second procedure, we simulate an in vivo experiment in which myogenic response is induced via drug application. Because myogenic constriction requires influx of  $Ca^{2+}$  into the SMC, the extracellular environment in the perivascular space is affected by dilations involving myogenic relaxation; namely, the perivascular  $Ca^{2+}$  concentration increases, which may affect the astrocytic TRPV4 channels. Thus, it is important to study the astrocyte response to arteriole dilations due to myogenic relaxation in addition to mechanical stretching. Experimentally, application of the drug pinacidil stimulates myogenic vessel dilations by activating KIR channels (Cao, 2011) in the vascular SMC, leading to a decrease in SMC intracellular  $Ca^{2+}$ . We simulate

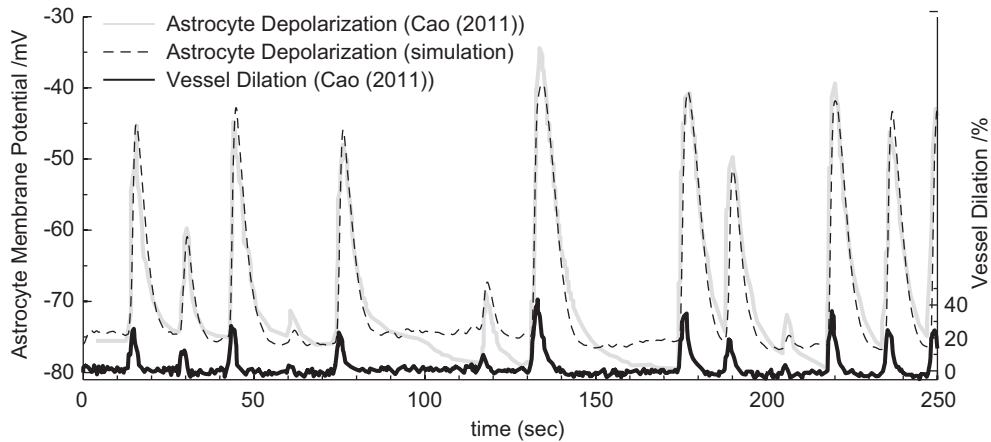


**Fig. 3.** Astrocyte response to mechanical stretching of vessel. Thick curves are experimental in vitro data extracted from Cao (2011, Chapter 4, Fig. 2); thick black curve is the vessel radial strain (20–40% of vessel radius); thick grey curve is the astrocyte membrane potential. Simulation data are shown as the black dotted line. The vessel dilations used in the simulation were interpolated from the data extracted from Cao (2011).

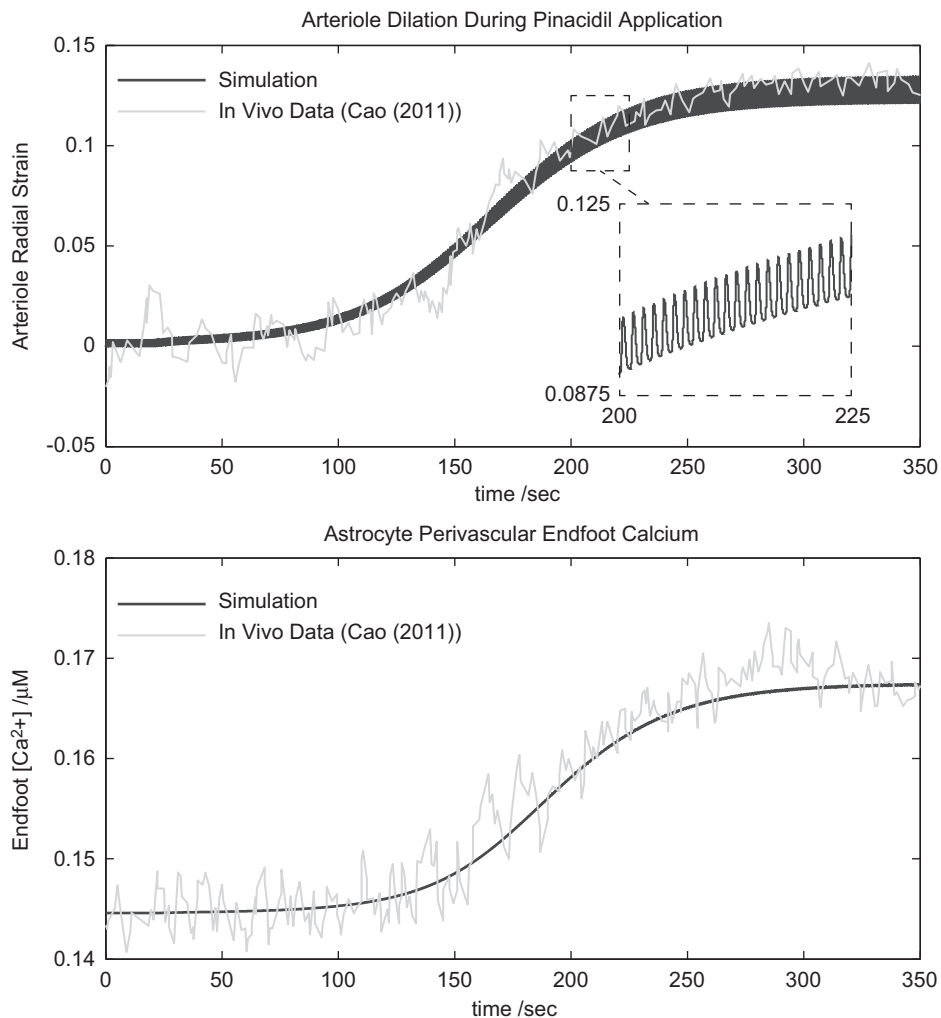


**Fig. 4.** Astrocyte response to drug induced vasodilation. Upper plot shows vessel radius in response to application of pinacidil; inset shows zoomed-in view for better resolution of vasomotion. Lower plot shows astrocyte intracellular  $Ca^{2+}$  concentration increasing in response to vessel dilation. Grey curves are data extracted from Cao (2011, Chapter 4, Fig. 7A). Black curves are simulation results.

the effect of this drug by enforcing a set KIR channel open population, and we compare the results to the in vivo data from Cao (2011).

All differential equations were solved in MATLAB using the solver “ode23tb,” which implements TR-BDF2, an implicit Runge–Kutta formula with backward differentiation (BDF).

### 3.2. TRPV4 model validation

Fig. 3 shows the astrocyte membrane depolarization in response to quick, mechanical stretches in the radial direction. The simulation was intended to mimic the in vitro experiment by Cao (2011) in which an arteriole in a brain slice was pressurized in brief bursts that inflated it between 20% and 40%. Data extracted from Cao (2011) are shown as thick black curves (vessel dilation) and thick grey curves (astrocyte membrane potential). In the simulation, the imposed strain on the vessel radius was interpolated from the extracted data. The black dotted line is the simulated astrocyte depolarization, which is in good agreement with the experimental results.

The astrocyte response is characterized by a quick rise –  $\sim 2$  s – to maximum depolarization, followed by a slow decay:  $\sim 4$  s to decay to half maximum, and  $\sim 15$  s to recover to baseline. Note that these simulation results are a product of the TRPV4 channel equations included in the model perivascular astrocyte endfoot, so the results in Fig. 3 support the hypothesis that TRPV4 channels are responsible for the astrocyte depolarization observed in response to vessel perturbations.

We further validate the model by simulating application of the vasodilatory drug pinacidil and compute the resulting  $\text{Ca}^{2+}$  concentration in the astrocyte, analogous to the in vivo experiment by Cao (2011). Pinacidil induces vasodilation by opening the KIR channels in the vascular smooth muscle cell (Cao, 2011). Further, data have suggested that pinacidil only affects the vascular SMC, and has no direct effect on neurons and astrocytes (Cao et al., 2009). We simulated the effect of pinacidil by imposing the SMC KIR channel open state,  $k$  (see Eq. (24)), directly. In order to reproduce the same vessel dilation as the analogous in vivo experiment by Cao (2011) (extracted data shown in Fig. 4, lower plot), we estimated that the pinacidil induced KIR activation progressed according to

$$k(t) = 0.01 \left( 1 + \tanh \frac{t-270}{60} \right), \quad (40)$$

where  $t$  is the time in seconds. For this simulation, Eq. (40) is substituted into Eq. (24) instead of solving for  $k$  with the ODE in Eq. (27).

The results are shown in Fig. 4; the lower plot is the arteriole dilation due to pinacidil application, and the upper plot is the resulting  $\text{Ca}^{2+}$  level in the adjacent perivascular astrocyte end-foot. As the vessel dilates, it activates the TRPV4 channels on the astrocyte perivascular endfoot, initiating a  $\text{Ca}^{2+}$  influx into the astrocyte. Again, the simulation (black curves) shows good agreement with experimental results (grey curves, extracted from Cao, 2011).

### 3.3. Astrocytic and vascular bidirectional interaction

The results in the whole system when the astrocyte is given a transient input of synaptic glutamate and  $\text{K}^+$  are shown in Fig. 5. The astrocytic  $\text{IP}_3$  immediately increases (Fig. 5(b)), while the subsequent rise in intracellular  $\text{Ca}^{2+}$  experiences a brief ( $< 1$  s) delay (Fig. 5(c)). The EET rise (Fig. 5(d)) follows that of  $\text{Ca}^{2+}$ . All three reach steady state within  $\sim 10$  s, while (Fig. 5(e)) the astrocyte continues to depolarize due to the influx of  $\text{K}^+$  from the synaptic space, which is eventually balanced by the  $\text{K}^+$  outflux due to  $\text{Ca}^{2+}$ - and EET-dependent opening of the BK channels in the perivascular endfoot. The  $\text{K}^+$  concentration (Fig. 5(f)) in the perivascular space activates arteriolar SMC KIR channels, further increasing the perivascular  $\text{K}^+$ , and causing a hyperpolarization of the SMC membrane (not shown) as well as damping the oscillations in the SMC  $\text{Ca}^{2+}$  and vessel radius. The hyperpolarization closes  $\text{Ca}^{2+}$  channels in the SMC, reducing the SMC  $\text{Ca}^{2+}$  concentration (Fig. 5(g)), thereby causing vessel dilation (Fig. 5(h)). As the perivascular  $\text{K}^+$  concentration continues to increase during stimulation, the dilated vessel contracts slowly due to the  $[\text{K}^+]_p$ -dependent shift in the KIR channel reversal potential, which reverses the direction of the  $\text{K}^+$  flow in the KIR channels and changes the polarity of the vessel response.

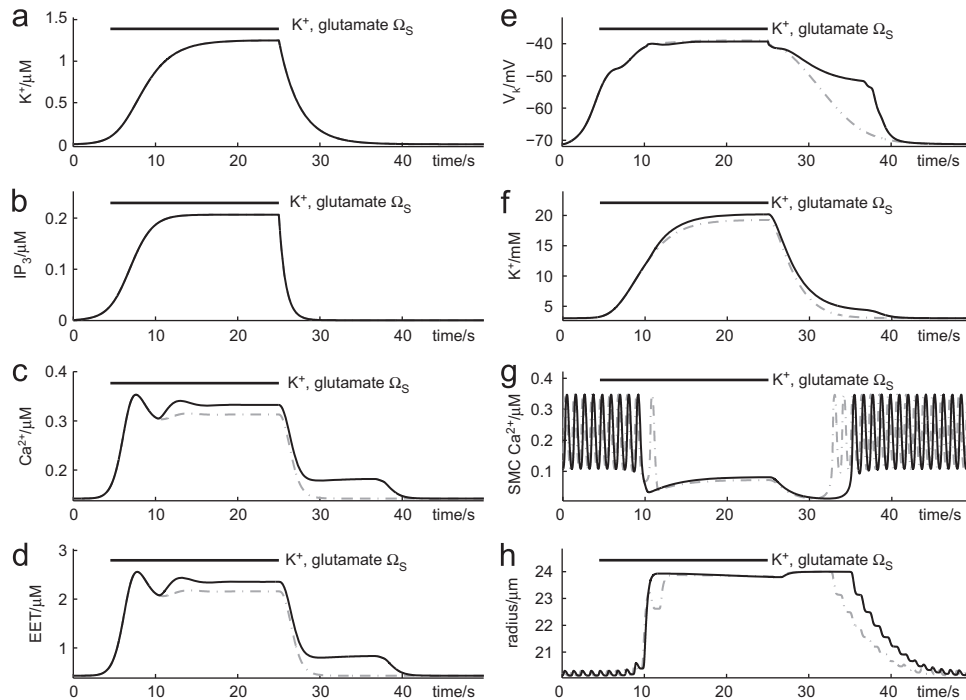


**Fig. 5.** Astrocytic and vascular bidirectional response during neural stimulation. Horizontal black bars indicate period of synaptic  $\text{K}^+$  and glutamate stimulus. Solid lines are results using the equations above. Dashed grey lines are results when TRPV4 channels are excluded from the model. (a)  $\text{K}^+$  concentration in synaptic space. (b) Astrocytic intracellular  $\text{IP}_3$  concentration. (c) Astrocytic intracellular  $\text{Ca}^{2+}$  concentration. (d) Astrocytic intracellular EET concentration. (e) Astrocyte membrane potential. (f) Extracellular  $\text{K}^+$  concentration in the perivascular space. (g) Arteriolar SMC intracellular  $\text{Ca}^{2+}$  concentration. (h) Arteriole radius.

The vessel dilation stretches the enclosing astrocytic endfoot, opening the stretch-gated TRPV4 channels in the membrane, causing an influx of  $Ca^{2+}$  into the astrocyte (Fig. 5(c)). After the stimulus, the vessel maintains its dilation until the remaining  $K^+$  in the perivascular space decays close to its baseline value.

There are two notable differences that arise in the simulation results due to our addition of the TRPV4 channel equations. The first is that the vessel response (Fig. 5(g) and (h)) in the TRPV4 model (black lines) is both prolonged and it rises to maximum dilation faster than when TRPV4 channels are excluded (grey lines). This is a result of the second difference, which is that the astrocytic TRPV4-mediated  $Ca^{2+}$  influx maintains the astrocytic  $Ca^{2+}$  signal and resulting EET production and BK channel activity (Fig. 5(c), (d), (e), black curves) until the vessel reconstricts, well past the end of the neural stimulus. In contrast, without TRPV4 channels included (grey curves), the astrocyte activity drops to baseline as soon as the neural stimulus ends, even while the vessel remains dilated. In this way, our model (with TRPV4 channels) predicts a more physiological result, consistent with the experimental data from Filosa et al. (2004). Notice that while the grey curves drop to baseline within seconds of the end of the neural stimulus, the black curves remain steady and drop to baseline just after 40 s, about the time that the vessel has returned to its initial level of constriction.

Shown in Fig. 5(g) and (h) are the SMC intracellular  $Ca^{2+}$  and vessel radius, respectively. (The same data are also shown in Fig. 7(b) and (d), where the astrocytic intracellular  $Ca^{2+}$  is superimposed for clarity on the SMC  $Ca^{2+}$  plot in Fig. 7(b).) Before the onset of the stimulus, the vessel experiences vasomotion: note the oscillating behavior in the absence of neural activity. In periods without neural stimuli, the amplitude and frequency ( $\sim 0.5$  Hz) of the oscillations are consistent with those observed in experiment (Filosa et al., 2004; Hundley et al., 1988; Morita-Tsuzuki et al., 1992; Lefer et al., 1990). During neural stimulation, the vessel dilates, and vasomotion is inhibited – note the flat, non-oscillatory response in the SMC  $Ca^{2+}$  and vessel radius while the vessel is in the dilated state. This phenomenon is

consistent with the experimental results of Filosa et al. (2004), Brown et al. (2002), Rivadulla et al. (2011). Dilation along with suppression of vasomotion occurs in response to the hyperpolarization that the SMC experiences when astrocytic  $K^+$  release activates the SMC KIR channels. This hyperpolarization closes SMC  $Ca^{2+}$  channels, preventing influx of  $Ca^{2+}$ . The reduction in intracellular  $Ca^{2+}$  allows myogenic relaxation, resulting in vasodilation (Fig. 5(h)). Further, the hyperpolarization suppresses  $Ca^{2+}$  oscillations in the SMC, thus suppressing radius oscillations (Fig. 5(g) and (h)). Note that vasomotion resumes after the termination of the functional hyperemia response, which is also observed experimentally (Filosa et al., 2004; Brown et al., 2002).

### 3.4. Sensitivity analysis of KIR channel model

Because the results from Farr and David (2011) show a non-physiological delay of  $\sim 20$  s in the vessel response, we adopt a modified set of parameters for the SMC KIR channel component of the model, which determines the way the vessel responds to astrocyte signals. We begin by investigating parametric sensitivity using the standard ANOVA decomposition (Yang et al., 2012). Fig. 6 shows the sensitivity of the response start time ( $\times$ ,  $t_1$ ), stop time ( $\bullet$ ,  $t_3$ ), and time at which the vessel response reverses direction during sustained stimulation ( $\circ$ ,  $t_2$ , see Fig. 6, inset). The most sensitive parameter is  $\nu_{KIR,2}$ , the baseline value of the  $[K^+]_P$ -dependent KIR reversal potential (Eq. (26)).

When we change  $\nu_{KIR,2}$  in order to decrease  $t_1$  to a more physiological value, at the same time,  $t_2$  would also decrease to a value too early to be physiologically meaningful: the vessel would respond quickly to the stimulus, but would immediately begin to reconstrict, while experimental results suggest that constrictive response should occur after longer periods of stimulation, when the perivascular  $K^+$  concentration has had time to increase above  $\sim 20$  mM (Horiuchi et al., 2002; Filosa et al., 2006). Thus, when adjusting the speed of the response by changing the value of  $\nu_{KIR,2}$ , we need an additional parameter change that would

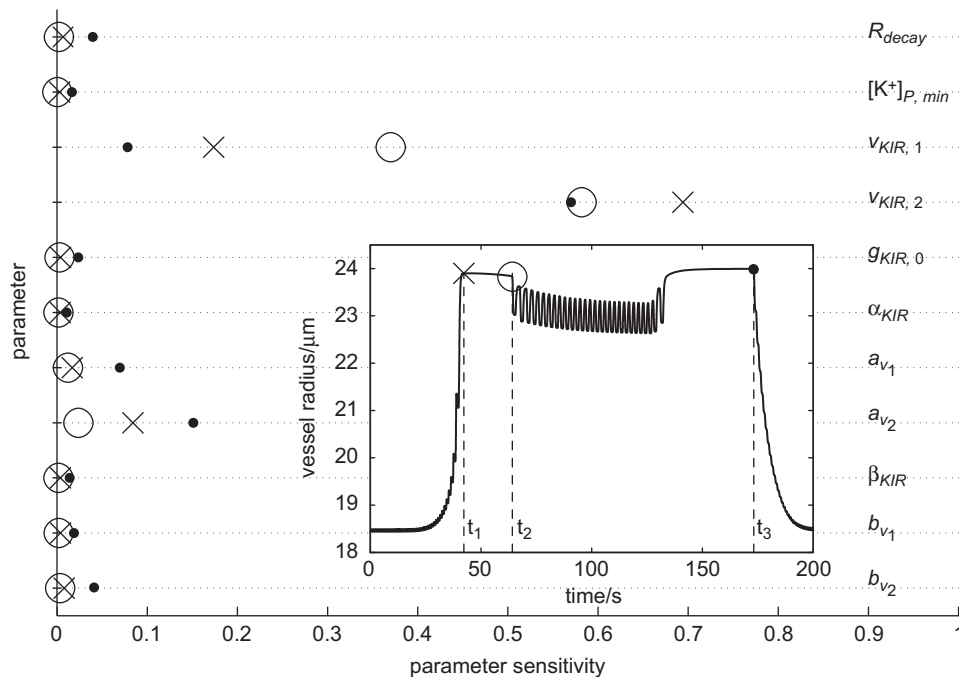


**Fig. 6.** KIR channel model parameter sensitivity using ANOVA of ( $\times$ )  $t_1$ —start time of vessel response, ( $\circ$ )  $t_2$ —time at which vessel response reverses and vessel reconstricts during stimulus, and ( $\bullet$ )  $t_3$ —end time of vessel response.

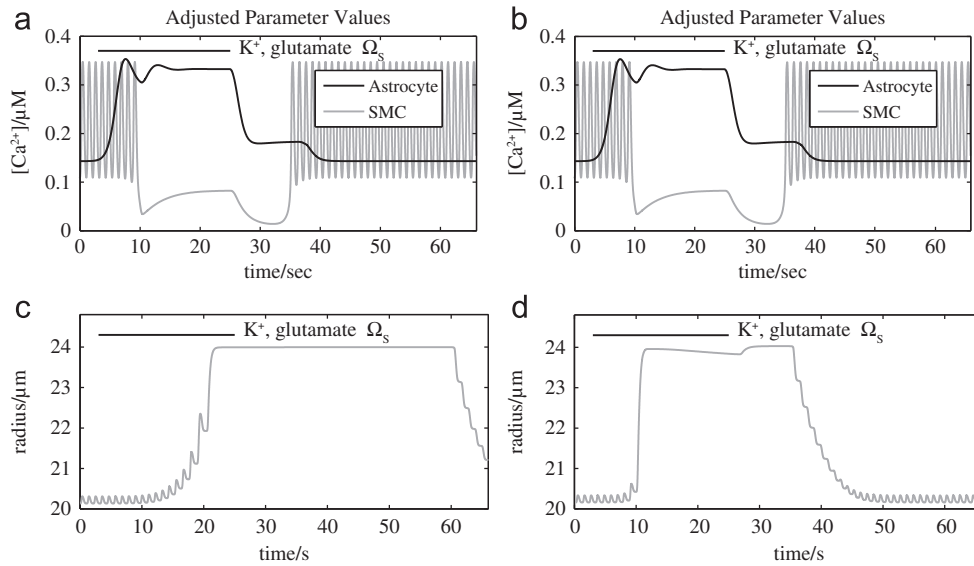


**Fig. 7.** Reaction timing. Horizontal black bars indicate period of synaptic  $K^+$  and glutamate stimulus. Original parameter values produce a delay ( $\sim 20$  s) in vessel response: (a) Astrocyte and SMC intracellular  $[Ca^{2+}]$ . (b) Vessel dilation. Adjusted parameters produce a response with a more physiological delay: ( $\sim 5$  s). (c) Astrocyte and SMC intracellular  $[Ca^{2+}]$ . (d) Vessel dilation (compare with Figs. 5A, C in Filosa et al., 2004).

maintain  $t_2$  at a physiological value. We first considered  $v_{KIR,1}$ , the second most sensitive parameter, but found it is similar to  $v_{KIR,2}$ , so any corrections in  $t_2$  would be accompanied by an unwanted increase in  $t_1$ .  $a_{v_2}$ , the third most sensitive parameter, has the opposite effect: when we adjust its value, we correct the resulting value of  $t_2$  while further decreasing  $t_1$ . In order to prevent the vessel from having too late of a response end time ( $t_3$ ) because of the first two parameter adjustments, we also adjust the value of  $R_{decay}$ , which is the only parameter to which  $t_3$  exclusively is sensitive. Because the original value of  $R_{decay}$  was an estimation (Farr and David, 2011), we felt that it would be acceptable to change it in order to find a closer match with the model results and experiment. Likewise, the values of  $v_{KIR,2}$  and  $a_{v_2}$  were originally taken from the models of coronary vessels; we believe it is reasonable that these values would be different in the brain, as the vascular morphology and function vary significantly across different specialized organs. We considered changing  $[K^+]_{p,min}$ , but the value of this parameter is known experimentally to be close to 3 mM in the brain (Kofuji and Newman, 2004), so it is more meaningful to leave this at the physiological value. Fig. 7 shows the results of the model before and after implementing the above parameter adjustments. The upper plots show the astrocytic and SMC  $Ca^{2+}$  concentration, and the lower plots show the vessel radius. Like the results from Farr and David (2011), the original parameter values (Fig. 7(a) and (c)) produce a large delay ( $\sim 20$  s) between the initial astrocytic  $Ca^{2+}$  rise and the vessel response time ( $t_1$ ). The results after adjusting the parameter values are shown in Fig. 7(b) and (d), where the delay between the astrocyte  $Ca^{2+}$  rise and  $t_1$  is  $\sim 5$  s, which is very close to experimental observations (Filosa et al., 2004, Fig. 6).

#### 4. Discussion

We have developed a set of equations and obtained parameters that reproduce experimental results of both astrocyte response to vasodilation (Cao, 2011) and suppression of vasomotion during functional hyperemia (Filosa et al., 2004; Brown et al., 2002; Rivadulla et al., 2011) with good qualitative agreement. We show that astrocyte mediated, neural induced vasodilation is accompanied by a reversible suppression of vasomotion in the

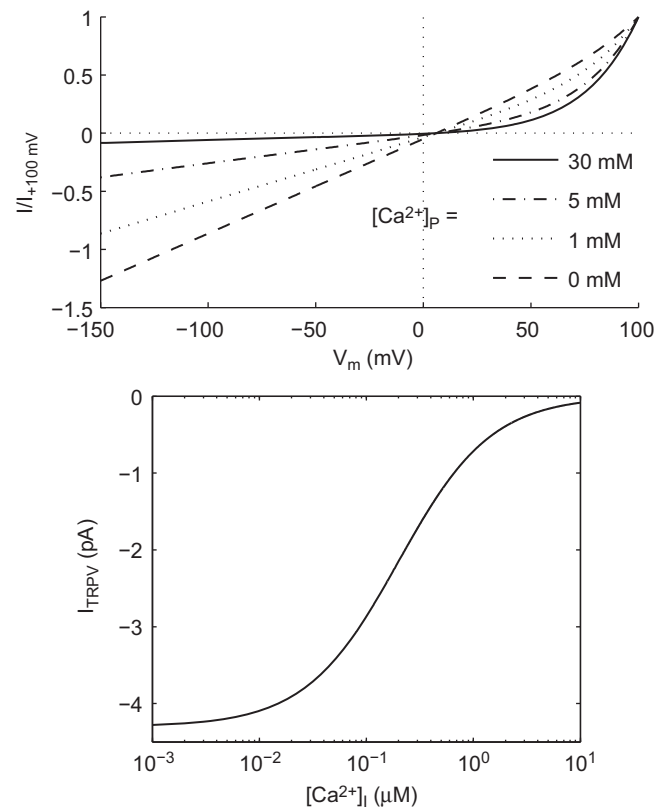


**Fig. 8.** Steady state inhibition of TRPV4 by  $Ca^{2+}$ . (Top) Current–voltage relationship for TRPV4 channel at different levels of extracellular (perivascular)  $Ca^{2+}$ . Curves are normalized to TRPV4 current at +100 mV. Compare with Fig. 6 in Nilius et al. (2004). (Bottom) TRPV4 current vs. astrocytic intracellular  $[Ca^{2+}]$ . Membrane potential is held at  $-80$  mV. Compare with Fig. 4B in Watanabe et al. (2003).

arteriole. Additionally, our model reproduces experimental observations of astrocyte  $Ca^{2+}$  increase and depolarization in response to vessel dilations.

The model description for  $Ca^{2+}$  gating properties of the TRPV4 channel is consistent with the experimental results of Watanabe

et al. (2003) and Nilius et al. (2004). Fig. 8 (top) shows the current–voltage relationship for the TRPV4 channel at different levels of perivascular  $\text{Ca}^{2+}$ . At high concentrations, the channel current is inhibited especially at negative voltages. These curves are a good match with the experimental results of Nilius et al. (2004). Fig. 8 (bottom) shows the inhibitory effect of intracellular  $\text{Ca}^{2+}$  on the TRPV4 channel current at a fixed membrane potential of  $-80$  mV. The values shown in the curve are a good match with experimental results (see Watanabe et al., 2003, Fig. 4).

In previous astrocyte models (e.g. Bennett et al., 2008; Farr and David, 2011), which do not include TRPV4 channels or any other mechanism of information transfer from vasculature to astrocytes, the astrocytic  $\text{Ca}^{2+}$  concentration drops to baseline immediately after the neural signal ends, while the arteriole remains dilated for a short ( $\sim 20$ – $50$  s) period. This is not the case in experimental observations, where both the astrocyte  $\text{Ca}^{2+}$  increase and the vessel response are observed to extend past the end of the neural stimulus (Filosa et al., 2004) and return to baseline together. Because of our development of TRPV4 channel equations, our model is the first to predict, consistent with experiment, sustained astrocyte activity, including raised intracellular  $\text{Ca}^{2+}$ , which is maintained until the vessel reconstricts, rather than dropping at the end of the neural stimulus (Fig. 5(c), (g), (h)).

At the same time, there is still a discrepancy between the experimental results and our model prediction, as we were not able to reproduce the correct level of astrocytic  $\text{Ca}^{2+}$  after neural signaling. While our results predict a partial drop in astrocytic  $\text{Ca}^{2+}$  after the end of neural stimulus, Filosa et al. (2004) observe that the astrocytic  $\text{Ca}^{2+}$  remains at its peak value for several seconds after neural stimulation.

This difference could be explained by our treatment of the astrocyte as a single spatial point, rather than considering the diffusion of chemicals and ions through a spatially resolved cell. This means that our model gives equal weight to electrical fluxes at the perivascular endfoot and the distant perisynaptic endfeet when determining the membrane potential across the TRPV4 channels in the perivascular endfeet, and it also assumes an instant and entire transfer of  $\text{Ca}^{2+}$  at the soma to the perivascular endfoot. In this case, the model may have an unrealistic balance that favors the neural-induced contribution of  $\text{Ca}^{2+}$  at the perivascular endfoot over the vessel dilation-induced TRPV4 activation of  $\text{Ca}^{2+}$  influx. This would explain why the  $\text{Ca}^{2+}$  in the endfoot would drop at the end of a neural signal, rather than remaining at peak value, as it would if it were most responsive to the local mechanical stimuli.

Another important piece that may be missing in our TRPV4 model may be the complete diverse set of gating factors. In our model, we consider mechanical, voltage, and intra- and extracellular  $\text{Ca}^{2+}$  gating, but TRPV4 channels have been observed to respond to a variety of additional variables including EET (Fernandes et al., 2008; Nilius et al., 2003, 2004). Nilius et al. (2004) demonstrate that  $\text{IP}_3$  sensitizes TRPV4 channels to EET, although this effect is most noticeable in instances of low ( $\sim 0$ – $0.1$   $\mu\text{M}$ ) EET concentration (Fernandes et al., 2008), well below the levels predicted in our model in response to neural stimulation (Fig. 5(d)).

While this model is the first bidirectional astrocyte model, responding both to neural and vascular stimuli, the model does not include signaling between astrocytes, which is a limitation. This omission, the same assumption invoked in previous generations of astrocyte models (Bennett et al., 2008; Farr and David, 2011), is a simplification for computational reducibility. In future versions of this model, we intend to add astrocyte-to-astrocyte communication to the model.

The astrocytic  $\text{Ca}^{2+}$ ,  $\text{IP}_3$ , and EET levels during neural stimulation are consistent with those of Farr and David (2011) and

produce similar ( $\sim 15\%$ ) increases in vessel radius. This verifies that the arteriole model equations adapted from Gonzalez-Fernandez and Ermentrout (1994) are appropriate in the context of the  $\text{K}^+$  signaling model proposed by Farr and David (2011). Further, we have reproduced their model's effect in which moderate increases (up to  $\sim 10$ – $15$  mM) of  $\text{K}^+$  in the perivascular space initiates vasodilation, while higher concentrations ( $> 15$  mM) result in constriction.

The arteriole model equations produce oscillatory behavior known as vasomotion in the vessel as a response to transmural pressure. Our results show that astrocytic vasodilatory signals (namely perivascular  $\text{K}^+$  activation of SMC KIR channels) damp these oscillations (both in the radius and the SMC intracellular  $\text{Ca}^{2+}$  concentration), and that vasomotion is restored after the signaling terminates, which is consistent with the experimental results of Filosa et al. (2004) and Brown et al. (2002). This helps to support the hypothesis that functional hyperemia occurs through the suppression of  $\text{Ca}^{2+}$  oscillations in vascular SMC. Further, our model helps build our overall understanding of functional hyperemia by integrating this hypothesis into a larger mechanistic framework, wherein the cause of the damping is a hyperpolarization, caused by activation of KIR channels by astrocytic  $\text{K}^+$  release in the perivascular space.

Combined with the  $\text{K}^+$  signaling model from Farr and David (2011), we identify the existence of three branch points in the vessel response (see Fig. 9) to increasing extracellular  $\text{K}^+$  concentration: (1) with a small  $\text{K}^+$  increase in the perivascular space, the vessel dilates and the equilibrium behavior changes from oscillatory to flat; (2) after the first branch point the vessel radius remains constant despite small increases in perivascular  $\text{K}^+$  until the concentration reaches the second branch point, at which the vessel constricts; (3) when the perivascular  $\text{K}^+$  is increased to the third branch point, the vessel has constricted enough to resume vasomotion, and the vessel equilibrium behavior switches from flat back to oscillating.

Although our arteriole model does not include endothelial cells, they may contribute to the vascular response during astrocyte-induced dilation. The endothelium responds to shear stress from blood flow, effecting a decrease in the SMC calcium level, thus modulating vasomotion and tone (Koenigsberger et al., 2005, 2006). If endothelial cells were included in the model, the arteriole dilation in response to extracellular  $\text{K}^+$  may appear to be diminished because the SMC will be starting at a greater initial level of relaxation. In addition, the endothelial cells may help determine the point at which further increases in extracellular  $\text{K}^+$  will cause the vessel to reconstrict. We expect that a mathematical description of the endothelium, if added to this model, would govern the locations of the three branch points mentioned above.

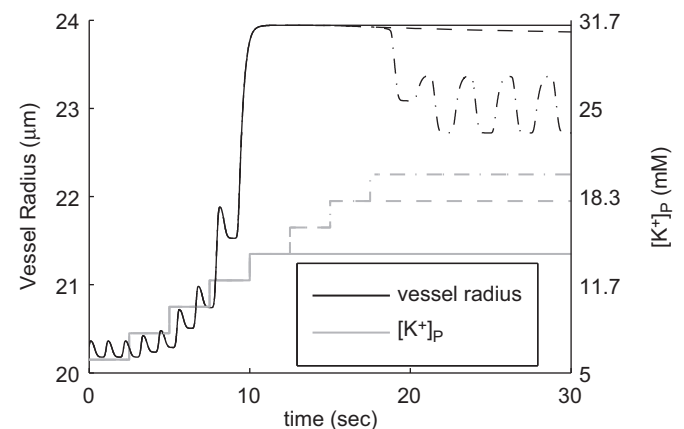


**Fig. 9.** Vessel branch points. With increasing  $[\text{K}^+]_p$ , the vessel transitions from vasomotion, to dilation with no oscillation (solid line), to constriction (dashed line), and back to vasomotion (dash-dot line).

However, while the endothelial layer is not explicitly included here, some of the influence of the endothelium on the SMC is accounted for by model parameters, particularly those involving the relation between the transmural pressure and the SMC  $\text{Ca}^{2+}$  level (see for example, Eq. (38)).

While there are experimental data documenting the presence of  $\text{Ca}^{2+}$ -permeable TRPV4 channels on astrocytic perivascular endfeet (Benfenati et al., 2007) and increases in intracellular  $\text{Ca}^{2+}$  in astrocytic perivascular endfeet in response to increases in vascular diameter (Cao, 2011), the subsequent effect of this response is unclear. It has been shown experimentally that  $\text{Ca}^{2+}$  increases in astrocytes are required for astrocytic glutamate release onto neurons (Bezzi et al., 1998; Hua et al., 2004; Malarkey et al., 2008; Halassa et al., 2007). However, while  $\text{Ca}^{2+}$  influx from extracellular space can contribute to astrocytic glutamate release, the  $\text{IP}_3$ -dependent  $\text{Ca}^{2+}$  release from internal stores is required for glutamate release (Hua et al., 2004). Thus, it is unlikely that the effect of  $\text{Ca}^{2+}$  influx through TRPV4 channels is glutamate release. One likely consequence of the TRPV4  $\text{Ca}^{2+}$  influx is to sustain the  $\text{Ca}^{2+}$ -dependent EET production and  $\text{K}^+$  release, thus extending the time over which vasodilation occurs (Koehler et al., 2006). As shown in Fig. 5, the model that includes TRPV4 channels has a much longer response in the vessel, which remains dilated for  $\sim 2$  s more than the model without astrocytic TRPV4 channels.

## 5. Conclusions and future work

We have simulated, for the first time, a bidirectional communication path between the cerebral microvasculature and astrocytes using  $\text{K}^+$  signaling from the astrocytes and astrocytic mechanosensation. The communication mechanisms involved in this model are chemical, electrical, and mechanical. Our results are physiologically consistent with other models and experiments. We were also able to simulate and predict the  $\text{Ca}^{2+}$  dynamics in an astrocyte as it responds to both neural and vascular inputs, which has not yet been investigated in depth experimentally.

We expect to achieve better physiological results by resolving our model spatially and including diffusion in the model equations. We intend to extend our model into an interactional network model in which signaling occurs between astrocytes, so that distant changes in the vasculature will have downstream consequences, both due to effects in blood flow and astrocytic crosstalk.

## Acknowledgments

We thank Drs. Jessica Filosa (Georgia Health Sciences University), Christopher Moore (Brown University), Les Farnell (University of Sydney), Bard Ermentrout (University of Pittsburgh), and Ms. Hannah Farr (University of Canterbury) for many helpful discussions. Simulations were performed on the CCV high performance computing cluster at Brown University. This work was supported by NSF OCI 0904288.

## Appendix A. Arteriole model equations

The equations that follow are adapted from Gonzalez-Fernandez and Ermentrout (1994), where they are discussed in further detail.

### A.1. Vessel SMC calcium concentration

The  $\text{Ca}^{2+}$  concentration in the SMC is governed by

$$\frac{d[\text{Ca}^{2+}]_{\text{SMC}}}{dt} = -\rho \left( \frac{1}{2\alpha} I_{\text{Ca}} + k_{\text{Ca}} [\text{Ca}^{2+}]_{\text{SMC}} \right), \quad (\text{A.1})$$

where  $I_{\text{Ca}}$  is the  $\text{Ca}^{2+}$  ion current (Eq. (36)),  $\alpha$  is the Faraday constant times cytosol volume (see Table B2);  $k_{\text{Ca}}$  is the constant ratio of  $\text{Ca}^{2+}$  outflux to influx, and  $\rho$  is

$$\rho = \frac{(K_d + [\text{Ca}^{2+}]_{\text{SMC}})^2}{(K_d + [\text{Ca}^{2+}]_{\text{SMC}})^2 + K_d B_T}, \quad (\text{A.2})$$

with  $K_d$  being the rate constant in the calcium buffer reaction and  $B_T$  is the total buffer concentration.

### A.2. Vessel mechanics

We consider a section of the vessel of length 1 cm (several orders of magnitude larger than the vessel diameter, which is  $\mu\text{m}$  scaled). The force on the vessel due to transmural pressure,  $\Delta p$ , is

$$f_{\Delta p} = \frac{1}{2} \Delta p \left( \frac{x}{\pi} - \frac{A}{x} \right), \quad (\text{A.3})$$

where the cross-sectional area is  $A = \pi(r_o^2 - r_i^2)$ , and the mean radius is  $\bar{r} = (r_o + r_i)/2$ , giving the mean circumference  $x = 2\pi\bar{r}$ .

For the muscle mechanics, consider a segment of the vessel as a cylindrical element with thickness  $r_o - r_i$ ,  $0 \leq \theta \leq 2\pi$ , and unit length along the axis. The longitudinal cross sectional surface area,  $S$ , is then  $S = 1(r_o - r_i)$ . The stresses on  $S$  are described using a Maxwell model along  $x$  (the mean circumference) that consists of a contractile component of length  $y$ , a series elastic component of length  $u$ , a parallel elastic component of length  $x = u + y$ , and a parallel viscous component (details in Gonzalez-Fernandez and Ermentrout, 1994). The hoop stresses associated with  $x$ ,  $y$ , and  $u$  are  $\sigma_x$ ,  $\sigma_y$ , and  $\sigma_u$ , respectively. The normalized hoop stresses in terms of the normalized lengths are

$$\sigma'_x = x'_3 \left( 1 + \tanh \frac{x' - x'_1}{x'_2} \right) + x'_4 (x' - x'_5) - x'_8 \left( \frac{x'_6}{x' - x'_7} \right)^2 - x'_9, \quad (\text{A.4})$$

$$\sigma'_u = u'_2 \exp(u'_1 u') - u'_3, \quad (\text{A.5})$$

and

$$\sigma'_y = \frac{\sigma_{y_0}}{\sigma_0^\#} \frac{\exp \left[ \left( \frac{-(y' - y'_0)^2}{2[y'_1/(y' + y'_2)]^{2y'_4}} \right) - y'_3 \right]}{1 - y'_3}. \quad (\text{A.6})$$

Here we consider nondimensional variables  $x' = x/x_0$ ,  $y' = y/x_0$ ,  $u' = u/x_0$ ,  $y'_0 = y_0/x_0$ , and similarly  $\sigma'_x = \sigma_x/\sigma_0^\#$ ,  $\sigma'_y = \sigma_y/\sigma_0^\#$ ,  $\sigma'_u = \sigma_u/\sigma_0^\#$ . The muscle-activation level  $\sigma_{y_0}$  comes from the attachment of myosin-actin crossbridges (Eq. (A.9)).

### A.3. Myogenic stress

The myogenic contraction occurs after the attachment of myosin and actin crossbridges, which involves the  $\text{Ca}^{2+}$ -dependent phosphorylation of the myosin chains. The ratio,  $\psi$ , of phosphorylated to total myosin chains is

$$\psi = \frac{[\text{Ca}^{2+}]_{\text{SMC}}^q}{C a_m^q + [\text{Ca}^{2+}]_{\text{SMC}}^q}, \quad (\text{A.7})$$

where  $C a_m$  and  $q$  are constants. The fraction of attached crossbridges,  $\omega$ , is governed by

$$\frac{d\omega}{dt} = k_\psi \left( \frac{\psi}{\psi_m + \psi} - \omega \right), \quad (\text{A.8})$$

where  $k_{psi}$  is the rate constant, and  $\psi_m$  is a constant. If the value of experimental  $[Ca^{2+}]_{SMC}$  associated with reference activation is  $Ca_{ref}$ , then

$$\sigma_{y_0} = \frac{\sigma_{y_0}^\#}{\omega_{ref}} \omega, \quad (A.9)$$

where  $\omega_{ref} = \psi(Ca_{ref}) / (\psi_m + \psi([Ca^{2+}]_{SMC,ref}))$ .

$$\frac{dy'}{dt} = \begin{cases} -v'_{ref} \frac{\psi}{\psi_{ref}} a' \frac{1 - \frac{\sigma'_u}{\sigma'_y}}{a' + \frac{\sigma'_u}{\sigma'_y}}, & 0 \leq \frac{\sigma'_u}{\sigma'_y} \leq 1, \\ c' \left[ \exp\left(b' \left(\frac{\sigma'_u}{\sigma'_y} - d'\right)\right) - \exp(b'(1-d')) \right], & 1 \leq \frac{\sigma'_u}{\sigma'_y}, \end{cases} \quad (A.10)$$

where  $v$  is the velocity of contraction of the contractile component at zero load, and  $v' = v/x_0$ , with  $v'_{ref}$  is  $v'$  at the reference muscle activation level. Similarly,  $\psi_{ref} = \psi(Ca_{ref})$ .

The hoop forces on  $S$  due to the viscoelastic and myogenic stress are

$$f_x = w_e S \sigma'_x \sigma_0^\#, \quad f_u = w_m S \sigma'_u \sigma_0^\#, \quad (A.11)$$

respectively. The weights,  $w_e$  and  $w_m$ , represent the contributions of the viscoelastic and myogenic hoop forces, respectively.

The circumferential contraction or dilation resulting from the forces on  $S$  is then

$$\frac{dx}{dt} = \frac{1}{\tau} (f_{\Delta p} - f_x - f_u), \quad (A.12)$$

where the time constant,  $\tau$ , is associated with the wall internal friction.

## Appendix B. Simulation parameters

Parameters used in this model are given in Tables B1 and B2. See Sections 2.2–2.4 for parameter descriptions; for parameters used in the vascular SMC equations, see Appendix A.

**Table B1**  
Astrocyte model parameters.

| $\Omega_s$ synaptic space                     |                            | Source                                                 |
|-----------------------------------------------|----------------------------|--------------------------------------------------------|
| $J_{SK,max} * k_{Na}$                         | 0.6 mM/s                   | Farr and David (2011)                                  |
| $KKO_a$                                       | 1.5 mM                     | Farr and David (2011)                                  |
| $\delta$                                      | 0.001235                   | Farr and David (2011)                                  |
| $K_G$                                         | 8.82                       | Farr and David (2011)                                  |
| $\Omega_{astr}$ astrocyte intracellular space |                            | Source                                                 |
| $r_h$                                         | 4.8 $\mu$ M                | Farr and David (2011)                                  |
| $k_{deg}$                                     | 1.25 $s^{-1}$              | Farr and David (2011)                                  |
| $\beta_{cyt}$                                 | 0.0244                     | Farr and David (2011)                                  |
| $K_{inh}$                                     | 0.1 $\mu$ M                | Bennett et al. (2008)                                  |
| $k_{on}$                                      | 2 $\mu$ M $^{-1}$ $s^{-1}$ | Bennett et al. (2008)                                  |
| $J_{max}$                                     | 2880 $\mu$ M $s^{-1}$      | Bennett et al. (2008)                                  |
| $K_I$                                         | 0.03 $\mu$ M               | Bennett et al. (2008)                                  |
| $K_{act}$                                     | 0.17 $\mu$ M               | Bennett et al. (2008)                                  |
| $V_{max}$                                     | 20 $\mu$ M $s^{-1}$        | Bennett et al. (2008)                                  |
| $k_{pump}$                                    | 0.24 $\mu$ M               | Bennett et al. (2008)                                  |
| $P_L$                                         | 5.2 $\mu$ M $s^{-1}$       | Farr and David (2011)                                  |
| $[Ca^{2+}]_{min}$                             | 0.1 $\mu$ M                | Farr and David (2011)                                  |
| $V_{EET}$                                     | 72 $s^{-1}$                | Farr and David (2011)                                  |
| $k_{EET}$                                     | 7.1 $s^{-1}$               | Farr and David (2011)                                  |
| $C_{astr}$                                    | 40 pF                      | Farr and David (2011)                                  |
| $g_{leak}$                                    | 78.54 pS                   | Farr and David (2011)                                  |
| $v_{leak}$                                    | –70 mV                     | Farr and David (2011)                                  |
| $g_{BK}$                                      | 225.6 pS                   | Filosa et al. (2006)                                   |
| $v_{BK}$                                      | –95 mV                     | Farr and David (2011)                                  |
| $EET_{shift}$                                 | 2 mV $\mu$ M $^{-1}$       | Farr and David (2011)                                  |
| $v_4$                                         | 14.5 mV                    | Farr and David (2011)                                  |
| $v_5$                                         | 8 mV                       | Farr and David (2011)                                  |
| $v_6$                                         | –15 mV                     | Farr and David (2011)                                  |
| $\psi_n$                                      | 2.664 $s^{-1}$             | Farr and David (2011)                                  |
| $Ca_3$                                        | 400 nM                     | Farr and David (2011)                                  |
| $Ca_4$                                        | 150 nM                     | Farr and David (2011)                                  |
| $g_{TRPV}$                                    | 200 pS                     | Kung (2005)                                            |
| $v_{TRPV}$                                    | 6 mV                       | Benfenati et al. (2007)                                |
| $\kappa$                                      | 0.04                       | Fit to Cao (2011)                                      |
| $v_{1,TRPV}$                                  | 120 mV                     | Fit to Nilius et al. (2004) and Watanabe et al. (2003) |
| $v_{2,TRPV}$                                  | 13 mV                      | Nilius et al. (2004) and Watanabe et al. (2003)        |
| $\epsilon_{1/2}$                              | 0.16                       | Fit to Cao (2011)                                      |
| $\gamma_{Ca_i}$                               | 0.2 $\mu$ M                | Watanabe et al. (2003)                                 |
| $\gamma_{Ca_e}$                               | 0.2 mM                     | Fit to Nilius et al. (2004)                            |
| $\tau_{TRPV}$                                 | 0.9 $s^{-1}$               | Fit to Cao (2011) and Watanabe et al. (2003)           |
| $\Omega_p$ perivascular space                 |                            | Source                                                 |
| $[Ca^{2+}]_{p,min}$                           | 2000 $\mu$ M               | Estimation                                             |
| $VR_{pa}$                                     | 3.2e–05                    | Farr and David (2011)                                  |

**Table B1** (continued)

| $\Omega_s$ synaptic space               |                                     | Source                      |
|-----------------------------------------|-------------------------------------|-----------------------------|
| $VR_{ps}$                               | 0.1                                 | Farr and David (2011)       |
| $R_{decay}$                             | $1 \text{ s}^{-1}$                  | See Section 3.4             |
| $Ca_{decay}$                            | $0.5 \text{ s}^{-1}$                | Estimation                  |
| $[K^+]_{p,min}$                         | 3 mM                                | Farr and David (2011)       |
| $\Omega_{SMC}$ smooth muscle cell space |                                     | Source                      |
| $v_{KIR,1}$                             | 57 mV                               | Farr and David (2011)       |
| $v_{KIR,2}$                             | 130 mV                              | See Section 3.4             |
| $g_{KIR,0}$                             | 145 pS                              | Farr and David (2011)       |
| $\alpha_{KIR}$                          | 1020 s                              | Farr and David (2011)       |
| $a_{v_1}$                               | 18 mV                               | Farr and David (2011)       |
| $a_{v_2}$                               | 10.8 mV                             | See Section 3.4             |
| $\beta_{KIR}$                           | 26.9 s                              | Farr and David (2011)       |
| $b_{v_1}$                               | 18 mV                               | Farr and David (2011)       |
| $b_{v_2}$                               | 0.06 mV                             | Farr and David (2011)       |
| $\gamma$                                | $1970 \text{ mV } \mu\text{M}^{-1}$ | Koenigsberger et al. (2006) |

**Table B2**

Arteriole model parameters.

| $\Omega_{SMC}$ smooth muscle cell space |                                | Source                                          |
|-----------------------------------------|--------------------------------|-------------------------------------------------|
| $A_p$                                   | 60 mmHg                        | Horiuchi et al. (2002) and Hudetz et al. (1987) |
| $v_1$                                   | -21.0 mV                       | See Eq. (38)                                    |
| $v_2$                                   | 25 mV                          | Gonzalez-Fernandez and Ermentrout (1994)        |
| $v_4$                                   | 14.5 mV                        | Gonzalez-Fernandez and Ermentrout (1994)        |
| $v_5$                                   | 8 mV                           | Gonzalez-Fernandez and Ermentrout (1994)        |
| $v_6$                                   | -15 mV                         | Gonzalez-Fernandez and Ermentrout (1994)        |
| $Ca_3$                                  | 400 nM                         | Gonzalez-Fernandez and Ermentrout (1994)        |
| $Ca_4$                                  | 150 nM                         | Gonzalez-Fernandez and Ermentrout (1994)        |
| $\phi_n$                                | 2.664                          | Gonzalez-Fernandez and Ermentrout (1994)        |
| $v_L$                                   | -70 mV                         | Gonzalez-Fernandez and Ermentrout (1994)        |
| $v_K$                                   | -80 mV                         | Gonzalez-Fernandez and Ermentrout (1994)        |
| $v_{Ca}$                                | 80 mV                          | Gonzalez-Fernandez and Ermentrout (1994)        |
| $C$                                     | 19.635 pF                      | Gonzalez-Fernandez and Ermentrout (1994)        |
| $g_L$                                   | 62.832 pS                      | Gonzalez-Fernandez and Ermentrout (1994)        |
| $g_K$                                   | 251.33 pS                      | Gonzalez-Fernandez and Ermentrout (1994)        |
| $g_{Ca}$                                | 157 pS                         | Gonzalez-Fernandez and Ermentrout (1994)        |
| $K_d$                                   | 1000 nM                        | Gonzalez-Fernandez and Ermentrout (1994)        |
| $B_T$                                   | 10000 nM                       | Gonzalez-Fernandez and Ermentrout (1994)        |
| $\alpha$                                | $4.3987e+15 \text{ nM C}^{-1}$ | Gonzalez-Fernandez and Ermentrout (1994)        |
| $k_{Ca}$                                | $1.3568e+11 \text{ nM C}^{-1}$ | Gonzalez-Fernandez and Ermentrout (1994)        |
| $[Ca^{2+}]_{SMC,m}$                     | 500 nM                         | Gonzalez-Fernandez and Ermentrout (1994)        |
| $q$                                     | 3                              | Gonzalez-Fernandez and Ermentrout (1994)        |
| $[Ca^{2+}]_{SMC,ref}$                   | 510 nM                         | Gonzalez-Fernandez and Ermentrout (1994)        |
| $k_\psi$                                | 3.3                            | Gonzalez-Fernandez and Ermentrout (1994)        |
| $\sigma_{y_0}^\#$                       | $2.6e+06 \text{ dyne cm}^{-2}$ | Gonzalez-Fernandez and Ermentrout (1994)        |
| $\sigma_0^\#$                           | $3e+06 \text{ dyne cm}^{-2}$   | Gonzalez-Fernandez and Ermentrout (1994)        |
| $\psi_m$                                | 0.3                            | Gonzalez-Fernandez and Ermentrout (1994)        |
| $v_{ref}$                               | 0.24                           | Gonzalez-Fernandez and Ermentrout (1994)        |
| $a'$                                    | 0.28125                        | Gonzalez-Fernandez and Ermentrout (1994)        |
| $b'$                                    | 5                              | Gonzalez-Fernandez and Ermentrout (1994)        |
| $c'$                                    | 0.03                           | Gonzalez-Fernandez and Ermentrout (1994)        |
| $d'$                                    | 1.3                            | Gonzalez-Fernandez and Ermentrout (1994)        |
| $x'_1$                                  | 1.2                            | Gonzalez-Fernandez and Ermentrout (1994)        |
| $x'_2$                                  | 0.13                           | Gonzalez-Fernandez and Ermentrout (1994)        |
| $x'_3$                                  | 2.2443                         | Gonzalez-Fernandez and Ermentrout (1994)        |
| $x'_4$                                  | 0.71182                        | Gonzalez-Fernandez and Ermentrout (1994)        |
| $x'_5$                                  | 0.8                            | Gonzalez-Fernandez and Ermentrout (1994)        |
| $x'_6$                                  | 0.01                           | Gonzalez-Fernandez and Ermentrout (1994)        |
| $x'_7$                                  | 0.32134                        | Gonzalez-Fernandez and Ermentrout (1994)        |
| $x'_8$                                  | 0.88977                        | Gonzalez-Fernandez and Ermentrout (1994)        |
| $x'_9$                                  | 0.0090463                      | Gonzalez-Fernandez and Ermentrout (1994)        |
| $u'_1$                                  | 41.76                          | Gonzalez-Fernandez and Ermentrout (1994)        |
| $u'_2$                                  | 0.047396                       | Gonzalez-Fernandez and Ermentrout (1994)        |
| $u'_3$                                  | 0.0584                         | Gonzalez-Fernandez and Ermentrout (1994)        |
| $y'_0$                                  | 0.928                          | Gonzalez-Fernandez and Ermentrout (1994)        |
| $y'_1$                                  | 0.639                          | Gonzalez-Fernandez and Ermentrout (1994)        |
| $y'_2$                                  | 0.35                           | Gonzalez-Fernandez and Ermentrout (1994)        |

Table B2 (continued)

| $\Omega_{SMC}$ smooth muscle cell space | Source                    |                                          |
|-----------------------------------------|---------------------------|------------------------------------------|
| $y'_3$                                  | 0.78847                   | Gonzalez-Fernandez and Ermentrout (1994) |
| $y'_4$                                  | 0.8                       | Gonzalez-Fernandez and Ermentrout (1994) |
| $x_0$                                   | 188.5 $\mu\text{m}$       | Ngai and Winn (1995)                     |
| $a$                                     | 50.265 $\mu\text{m}^2$    | Dacey and Duling (1982)                  |
| $S$                                     | 40 000 $\mu\text{m}^2$    | Dacey and Duling (1982)                  |
| $w_e$                                   | 0.9                       | Gonzalez-Fernandez and Ermentrout (1994) |
| $w_m$                                   | 0.7                       | Gonzalez-Fernandez and Ermentrout (1994) |
| $\tau$                                  | 0.2 dyne $\text{cm}^{-1}$ | Gonzalez-Fernandez and Ermentrout (1994) |

## References

- Barres, B.A., Koroshetz, W.J., Chun, L.L.Y., Corey, D.R., 1990. Ion channel expression by white matter glia: the type-1 astrocyte. *Neuron* 5 (4), 527–544.
- Benfenati, V., Amiry-Moghaddam, M., Caprini, M., Mylonakou, M.N., Rapisarda, C., Ottersen, O.P., Ferroni, S., 2007. Expression and functional characterization of transient receptor potential vanilloid-related channel 4 (TRPV4) in rat cortical astrocytes. *Neuroscience* 148, 876–892.
- Bennett, M.R., Farnell, L., Gibson, W., 2008. Origins of blood volume change due to glutamatergic synaptic activity at astrocytes abutting on arteriolar smooth muscle cells. *J. Theor. Biol.* 250, 172–185.
- Bezzi, P., Carmignoto, G., Pasti, L., Vesce, S., DanielaRossi, Rizzini, B.L., 1998. Prostaglandins stimulate calcium-dependent glutamate release in astrocytes. *Nature* 391 (January), 281–285.
- Brown, L., Key, B., Lovick, T., 2002. Inhibition of vasomotion in hippocampal cerebral arterioles during increases in neuronal activity. *Autonomic Neurosci.: Basic Clin.* 95, 137–140.
- Cao, R., 2011. The Hemo-neural Hypothesis: Effects of Vasodilation on Astrocytes in Mammalian Neocortex. Ph.D. Thesis. Department of Brain & Cognitive Sciences, Massachusetts Institute of Technology, Cambridge, MA, February.
- Cao, R., Higashikubo, B.T., Cardin, J., Knoblich, U., Ramos, R., Nelson, M.T., Moore, C.I., 2009. Pinacidil induces vascular dilation and hyperemia in vivo and does not impact biophysical properties of neurons and astrocytes in vitro. *Cleveland Clin. J. Med.* 76 (April), S80–S85.
- Dacey Jr., R.G., Duling, B.R., 1982. A study of rat intracerebral arterioles: methods, morphology, and reactivity. *Am. J. Physiol.* 243, H598–H606.
- Farr, H., David, T., 2011. Models of neurovascular coupling via potassium and EET signalling. *J. Theor. Biol.* 286, 13–23.
- Fernandes, J., Lorenzo, I.M., Andrade, Y.N., Garcia-Elias, A., Serra, S.A., Fernández-Fernández, J.M., Valverde, M.A., 2008. IP3 sensitizes TRPV4 channel to the mechano- and osmotransducing messenger 5'-6'-epoxyeicosatrienoic acid. *J. Cell Biol.* 181 (April (1)), 143–155.
- Filosa, J.A., Bonev, A.D., Nelson, M.T., 2004. Calcium dynamics in cortical astrocytes and arterioles during neurovascular coupling. *Circ. Res.* 95 (October), e73–e81.
- Filosa, J.A., Bonev, A.D., Straub, S.V., Meredith, A.L., Wilkerson, M.K., Aldrich, R.W., Nelson, M.T., 2006. Local potassium signaling couples neuronal activity to vasodilation in the brain. *Nat. Neurosci.* 9 (11), 1397–1403.
- Gonzalez-Fernandez, J.M., Ermentrout, B., 1994. On the origin and dynamics of the vasomotion of small arteries. *Math. Biosci.* 119, 127–167.
- Haddock, R., Hirst, G., Hill, C., 2002. Voltage independence of vasomotion in isolated irideal arterioles of the rat. *J. Physiol.* 540 (1), 219–229.
- Halassa, M.M., Fellin, T., Takano, H., Dong, J.-H., Haydon, P.G., 2007. Synaptic islands defined by the territory of a single astrocyte. *J. Neurosci.* 27 (June (24)), 6473–6477.
- Hamill, O.P., Martinac, B., 2001. Molecular basis of mechanotransduction in living cells. *Physiol. Rev.* 81 (April (2)), 685–733.
- Haydon, P.G., Carmignoto, G., 2006. Astrocyte control of synaptic transmission and neurovascular coupling. *Physiol. Rev.* 86, 1009–1031.
- Higashi, K., Fujita, A., Inanobe, A., Tanemoto, M., Doi, K., Kubo, T., Kurachi, Y., 2001. An inwardly rectifying  $\text{K}^+$  channel, Kir4.1, expressed in astrocytes surrounds synapses and blood vessels in brain. *Am. J. Physiol. Cell Physiol.* 281 (3), C922–C931.
- Higashimori, H., Sontheimer, H., 2007. Role of Kir4.1 channels in growth control of glia. *Glia* 55 (16), 1668–1679.
- Horiuchi, T., Dietrich, H.H., Hongo, K., Dacey, R.G., 2002. Mechanism of extracellular  $\text{K}^+$ -induced local and conducted responses in cerebral penetrating arterioles. *Stroke* 33 (11), 2692–2699.
- Hua, X., Malarkey, E.B., Sunjara, V., Rosenwald, S.E., Hong Li, W., 2004.  $\text{Ca}^{2+}$ -dependent glutamate release involves two classes of endoplasmic reticulum  $\text{Ca}^{2+}$  stores in astrocytes. *J. Neurosci. Res.* 76 (March), 86–97.
- Hudetz, A.G., Conger, K.A., Halsey, J.H., Pal, M., Dohan, O., Kovach, A.G.B., 1987. Pressure distribution in the pial arterial system of rats based on morphometric data and mathematical models. *J. Cereb. Blood Flow Metab.* 7 (3), 342–355.
- Hundley, W.G., Renaldo, G.J., Levasseur, J.E., Kontos, H.A., 1988. Vasomotion in cerebral microcirculation of awake rabbits. *Am. J. Physiol. Heart Circ. Physiol.* 254 (January (1)), H67–H71.
- Koehler, R.C., Gebremedhin, D., Harder, D.R., 2006. Role of astrocytes in cerebrovascular regulation. *J. Appl. Physiol.* 100, 307–317.
- Koenigsberger, M., Sausser, R., Bény, J., Meister, J., 2005. Role of the endothelium on arterial vasomotion. *Biophys. J.* 88 (6), 3845–3854.
- Koenigsberger, M., Sausser, R., Bény, J.-L., Meister, J.-J., 2006. Effects of arterial wall stress on vasomotion. *Biophys. J.* 91 (September), 1663–1674.
- Kofuji, P., Newman, E.A., 2004. Potassium buffering in the central nervous system. *Neuroscience* 129 (4), 1043–1054.
- Kung, C., 2005. A possible unifying principle for mechanosensation. *Nature* 436 (August), 647–654.
- Lefler, D.J., Lynch, C.D., Lapinski, K.C., Hutchins, P.M., 1990. Enhanced vasomotion of cerebral arterioles in spontaneously hypertensive rats. *Microvasc. Res.* 39 (March (2)), 129–139.
- Malarkey, E.B., Ni, Y., Parpura, V., 2008.  $\text{Ca}^{2+}$  entry through TRPC1 channels contributes to intracellular  $\text{Ca}^{2+}$  dynamics and consequent glutamate release from rat astrocytes. *Glia* 56, 821–835.
- McCaslin, A.F., Chen, B.R., Radosevich, A.J., Cauliand, B., Hillman, E.M., 2011. In vivo 3D morphology of astrocyte-vasculature interactions in the somatosensory cortex: implications for neurovascular coupling. *J. Cereb. Blood Flow Metab.* 31, 795–806.
- Moore, C.I., Cao, R., 2008. The hemo-neural hypothesis: on the role of blood flow in information processing. *J. Neurophysiol.* 99, 2035–2047.
- Morita-Tsuzuki, Y., Bouskela, E., Hardebo, J.E., 1992. Vasomotion in the rat cerebral microcirculation recorded by laser-doppler flowmetry. *Acta Physiol. Scand.* 146 (December (4)), 431–439.
- Nedergaard, M., Ransom, B., Goldman, S.A., 2003. New roles for astrocytes: redefining the functional architecture of the brain. *Trends Neurosci.* 26 (10), 523–530.
- Ngai, A.C., Winn, H.R., 1995. Modulation of cerebral arteriolar diameter by intraluminal flow and pressure. *Circ. Res.* 77, 832–840.
- Nilius, B., Vriens, J., Prenen, J., Droogmans, G., Voets, T., 2004. TRPV4 calcium entry channel: a paradigm for gating diversity. *Am. J. Physiol. Cell Physiol.* 286, C195–C205.
- Nilius, B., Watanabe, H., Vriens, J., 2003. The TRPV4 channel: structure–function relationship and promiscuous gating behaviour. *Eur. J. Physiol.* 446, 298–303.
- Rivadulla, C., de Labra, C., Grieve, K.L., Cudeiro, J., 2011. Vasomotion and neurovascular coupling in the visual thalamus in vivo. *PLoS ONE* 6 (12), e28746.
- Watanabe, H., Vriens, J., Janssens, A., Wondergem, R., Droogmans, G., Nilius, B., 2003. Modulation of TRPV4 gating by intra- and extracellular  $\text{Ca}^{2+}$ . *Cell Calcium* 33, 489–495.
- Yang, X., Choi, M., Lin, G., Karniadakis, G.E., 2012. Adaptive ANOVA decomposition of stochastic incompressible and compressible flows. *J. Comput. Phys.* 231, 1587–1614.